Supplemental Material for "Anisotropic exchange within decoupled tetrahedra in the quantum breathing pyrochlore $Ba_3Yb_2Zn_5O_{11}$"*

J. G. Rau,[1,†] L. S. Wu,[2,‡] A. F. May,[3] L. Poudel,[2,4] B. Winn,[2] V. O. Garlea,[2] A. Huq,[5] P. Whitfield,[5] A. E. Taylor,[2] M. D. Lumsden,[2] M. J. P. Gingras,[1,6,7] and A. D. Christianson[2,4]

[1]*Department of Physics and Astronomy, University of Waterloo, Ontario, N2L 3G1, Canada*
[2]*Quantum Condensed Matter Division, Oak Ridge National Laboratory, Oak Ridge, TN-37831, USA*
[3]*Materials Science & Technology Division, Oak Ridge National Laboratory, Oak Ridge, TN-37831, USA*
[4]*Department of Physics & Astronomy, University of Tennessee, Knoxville, TN-37966, USA*
[5]*Chemical & Engineering Materials Division, Oak Ridge National Laboratory, Oak Ridge, TN 37831, USA*
[6]*Perimeter Institute for Theoretical Physics, Waterloo, Ontario, N2L 2Y5, Canada*
[7]*Canadian Institute for Advanced Research, 180 Dundas Street West, Suite 1400, Toronto, ON, M5G 1Z8, Canada*

(Dated: June 1, 2016)

I. SAMPLE SYNTHESIS

Polycrystalline samples of $Ba_3Yb_2Zn_5O_{11}$ were synthesized by solid-state reaction in Al_2O_3 crucibles. The high-purity reactants (dried Yb_2O_3, $BaCO_3$, ZnO) were ground together for 5-10 minutes using an agate milling set in a SPEX SamplePrep Mixer/Mill. The mixture was pressed into pellets, which were initially fired at 1150°C for 25-50 h (in air). Subsequent milling, pellet pressing, and annealing at temperatures up to 1170°C were utilized to promote homogeneity and phase purity in the final product. A slight excess (up to 4 at.%) of Ba and Zn-containing reactants was utilized to minimize the chance of forming Yb-containing impurities.

II. SPECIFIC HEAT AND MAGNETIC SUSCEPTIBILITY

Magnetization measurements were performed upon cooling in an applied field of 0.1 T, and isothermal magnetization measurements were performed at 1.9 K; Quantum Design's Magnetic Property Measurement System was utilized for magnetic measurements. Specific heat measurements were performed in a Quantum Design Physical Property Measurement System.

The specific heat of $Ba_3Yb_2Zn_5O_{11}$ is shown in Fig. S1. The specific heat of a sample from the same batch used for the inelastic neutron scattering measurements is compared with that from Kimura *et al.* [S1]. Both measurements are consistent with a maximum at ~ 2.4 K.

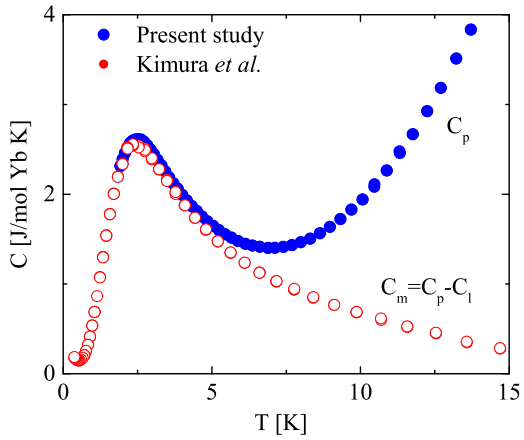

FIG. S1. The temperature dependent specific heat of $Ba_3Yb_2Zn_5O_{11}$. Filled circles are from measurements of a piece taken from the same batch as used for the inelastic neutron scattering measurements. Open circles are the magnetic contribution to the specific heat (C_m) taken from Kimura *et al.* [S1], determined C_m by subtracting the lattice contribution (C_l) estimated from $Ba_3Lu_2Zn_5O_{11}$ from the specific heat of $Ba_3Yb_2Zn_5O_{11}$ (C_p).

The magnetic susceptibility and inverse susceptibility of a sample taken from the same batch as the sample used for the inelastic neutron scattering data are shown in Fig. S2 for an applied field of 0.1 T. A maximum in the susceptibility occurs at ~ 4 K.

III. NEUTRON DIFFRACTION

Neutron powder diffraction measurements of $Ba_3Yb_2Zn_5O_{11}$ were performed with the time-of-flight powder diffractometer POWGEN, at the Spallation Neutron Source (SNS) at Oak Ridge National Laboratory [S2]. Data were collected on a powder $Ba_3Yb_2Zn_5O_{11}$ sample with mass 6.32 g. The data were collected for 2 hours at temperatures 10 K and 300 K, respectively. Structural refinement was carried out using the software package FULLPROF [S3]

† jeff.rau@uwaterloo.ca
‡ wul1@ornl.gov

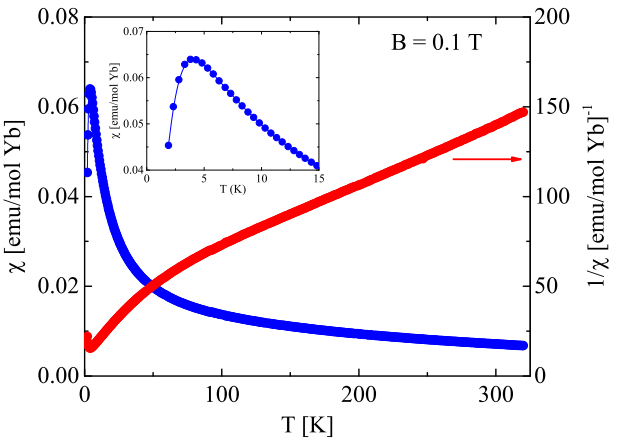

FIG. S2. Left axis: The temperature dependent static magnetic susceptibility ($\chi = M/B$) for $Ba_3Yb_2Zn_5O_{11}$ (blue circles), measured in field $B = 0.1$ T from temperature 1.9 to 320 K. Right axis: The inverse magnetic susceptibility ($1/\chi$) as a function of temperature. The inset shows an expanded view of the low temperature region, where a maximum in the susceptibility occurs around 4 K.

Atom	Wyckoff	x	y	z	B_{iso}	Occ.
Ba	24f	0.7055(3)	0.00000	0.00000	0.1313(0)	0.25000
Yb	16e	0.8365(5)	0.8365(5)	0.8365(5)	0.1187(9)	0.16670
Zn(1)	16e	0.0832(5)	0.0832(5)	0.0832(5)	0.1155(4)	0.16670
Zn(2)	24g	0.25000	0.25000	0.0828(1)	0.1729(2)	0.25000
O(1)	4b	0.50000	0.50000	0.50000	0.4219(9)	0.04167
O(2)	4a	0.00000	0.00000	0.00000	0.2334(2)	0.04167
O(3)	16e	0.3419(3)	0.3419(3)	0.3419(3)	0.3313(9)	0.16670
O(4)	16e	0.6679(6)	0.6679(6)	0.6679(6)	0.3777(2)	0.16670
O(5)	48h	0.1660(2)	0.1660(2)	1.0000(4)	0.30015(0)	0.50000

Atom	Wyckoff	x	y	z	B_{iso}	Occ.
Ba	24f	0.7055(6)	0.00000	0.00000	0.7268(4)	0.25000
Yb	16e	0.8365(5)	0.8365(5)	0.8365(5)	0.4480(3)	0.16670
Zn(1)	16e	0.0832(9)	0.0832(9)	0.0832(9)	0.4184(2)	0.16670
Zn(2)	24g	0.25000	0.25000	0.0824(7)	0.5697(8)	0.25000
O(1)	4b	0.50000	0.50000	0.50000	0.8089(3)	0.04167
O(2)	4a	0.00000	0.00000	0.00000	0.4878(2)	0.04167
O(3)	16e	0.3421(4)	0.3421(4)	0.3421(4)	0.6450(5)	0.16670
O(4)	16e	0.6683(0)	0.6683(0)	0.6683(0)	0.7374(4)	0.16670
O(5)	48h	0.1659(4)	0.1659(4)	1.0001(6)	0.6505(3)	0.50000

TABLE S1. Atomic parameters for $Ba_3Yb_2Zn_5O_{11}$ at 10 K (top panel) and 300 K (bottom panel).

The neutron diffraction data at 10 and 300 K along with the Rietveld refinement of the structural model is shown in Fig. S3(a) and (b) respectively. The fitted model describes the data well over a wide wave vector range ($1.3 < |\mathbf{Q}| < 21$ Å^{-1}). A few unindexed impurity peaks with intensities less than 1% of the main diffraction peaks of $Ba_3Yb_2Zn_5O_{11}$ are observed. The small fraction of impurities appears to be consistent with that found by Kimura *et al.* [S1] and indicates that the sample consists primarily of the cubic $Ba_3Yb_2Zn_5O_{11}$ phase. No site vacancies or disorder between sites was detected within experimental resolution (<2%). The refined atomic parameters of $Ba_3Yb_2Zn_5O_{11}$ at 10 K and 300 K are shown in Table S1. The lattice constants and goodness of fit parameters are displayed in Table S2.

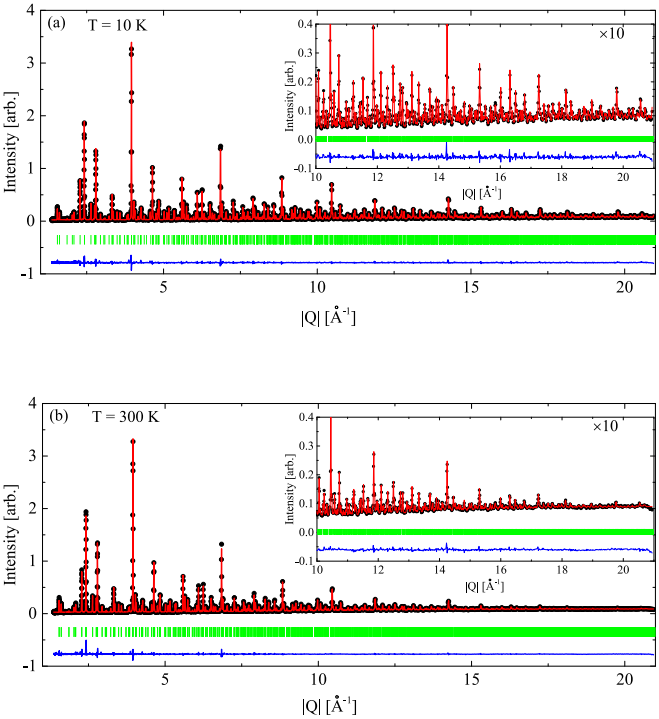

FIG. S3. Neutron powder diffraction data collected with POWGEN at 10 K (a) and 300 K (b) for $Ba_3Yb_2Zn_5O_{11}$. Rietveld refinement (red line), difference pattern (blue line) and calculated reflection positions (green ticks) are superimposed on the data points (black circles). The insets show an expanded view of the high $|\mathbf{Q}|$ region of the data.

T (K)	a (Å)	R_p	R_{wp}	R_{exp}	χ^2
10	13.47117(3)	9.07	8.63	1.53	31.8
300	13.48997(3)	10.7	9.23	1.99	21.5

TABLE S2. Comparison of the refinement parameters at 10 and 300 K.

IV. INELASTIC NEUTRON SCATTERING

Inelastic neutron scattering (INS) experiments were performed on the hybrid spectrometer (HYSPEC) at the Spallation Neutron Source at Oak Ridge National Laboratory [S5]. The data were collected at 0.25 K, 10 K, and 20 K utilizing a ^{3}He refrigerator, with incident energies $E_i = 3.8$, 7.5, and 15 meV and Fermi chopper frequencies of 180, 300, and 300 Hz respectively. To cover a large region of reciprocal space the center of the detector vessel, which covers 60° of scattering angle, was placed at scattering angles ranging from 33 - 101°.

Shown in Fig. S4(a), and Fig. S4(b) are the intensity maps of the inelastic neutron scattering data of $Ba_3Yb_2Zn_5O_{11}$ with $E_i = 15$ meV measured at temperatures 0.25 K and 10 K.

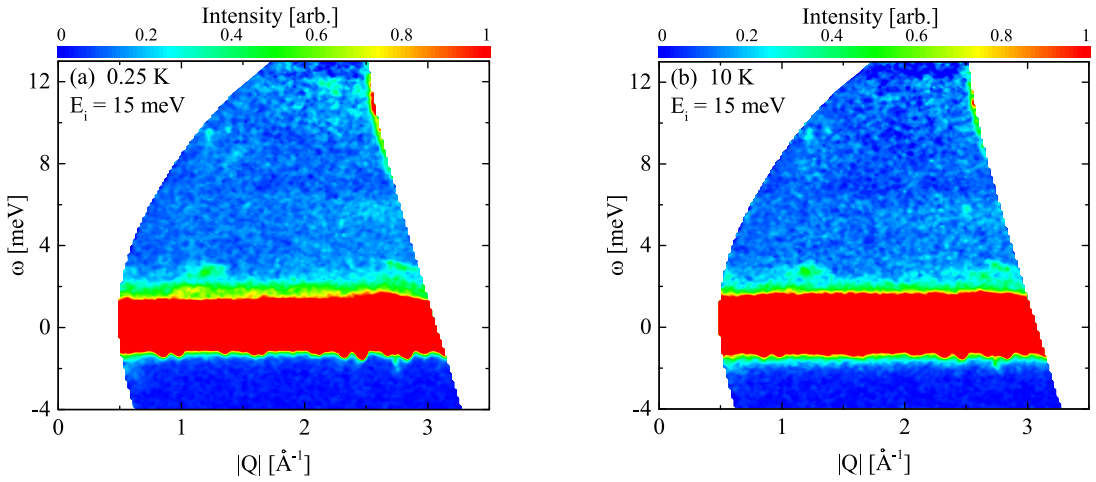

FIG. S4. Intensity map of the inelastic neutron scattering from $Ba_3Yb_2Zn_5O_{11}$ with $E_i = 15$ meV at 0.25 K (a) and 10 K (b).

Although the low energy excitations are not well resolved with $E_i = 15$ meV, the data shown in Fig. S4 confirm that there is no additional excitations up to 13.75 meV, which is consistent with the model described in the main text.

As mentioned in the main text, we noticed that there is a weak broad feature in the INS spectrum near an energy transfer of 1 meV (main text Fig. 2(a)). However, this feature has a significantly different dependence on wave vector $|\mathbf{Q}|$ from that of the other observed modes. Fig. S5(a) shows the wave vector $|\mathbf{Q}|$ dependent neutron scattering intensity measured at 0.25 K with incident energy $E_i = 3.8$ meV, averaged over the excitation energy window $\omega = [0.65, 0.9]$ meV and $\omega = [1, 1.25]$ meV. In contrast to the well defined inelastic mode contained in the energy range $\omega = [0.65, 0.9]$ meV, which peaks near $|\mathbf{Q}| = 1.3\text{Å}^{-1}$, the broad feature captured by the integration range, $\omega = [1, 1.25]$ meV is much weaker with a small peak around $|\mathbf{Q}| = 0.7\text{Å}^{-1}$. We were unable to identify any background from the instrument or the sample environment that could give the broad feature around $1 - 1.25$ meV in the HYSPEC neutron data. The statistics of the data is good, in particular the error bars on the data points in the $|\mathbf{Q}|$-dependence plot (see Fig. S5) are less than the symbol size. We note that to support this conclusion we have included additional data with $E_i = 7.5$ meV (see Fig. S5) that has a similar $|\mathbf{Q}|$-dependence. Additionally, the excitation is much broader than the other nearly resolution limited excitations observed. Within our theoretical model, there is no way to have these sharp modes, indicating excitations local to the tetrahedra, while simultaneously having such a broad mode at 1 meV. These incompatibilities, combined with the excellent agreement of theory and experiment with this mode excluded, lead us to ignore this feature.

As a supplement to the data collected at 0.25 K and 20 K with $E_i = 3.8$ meV described and shown in the main text, data collected with $E_i = 3.8$ meV at 10 K is shown in Fig. S6 below. The HYSPEC instrumental energy resolution with $E_i = 3.8$ meV and the 180 Hz chopper setting used experimentally is shown in Fig. S7 as a function of energy transfer. The $|\mathbf{Q}|$ dependence of the inelastic spectrum is shown through a series of cuts with an energy range of $[0.65, 0.9]$ meV at temperatures of 0.25, 10, and 20 K in Fig. S8.

V. CRYSTAL FIELD EXCITATIONS

Inelastic neutron scattering data was collected with the ARCS [S6] time-of-flight spectrometer to probe the excitation spectrum at higher energies, as shown in Fig. S9. This data was collected at 10 K with $E_i = 100$ meV and shows three crystal field excitations at $\sim$ 38, 54, and 67 meV. The data presented here are consistent with the results of Ref. [S7] where a more detailed analysis of the crystal field excitation spectrum and Hamiltonian can be found. We note that for a Kramers ion such as Yb^{3+} ($J = 7/2$), in the absence of broken time reversal symmetry, the minimum degeneracy is two so that $(2J + 1)/2$ doublets are expected including the ground state. Thus the observation of three crystal field excitations is strong evidence that the modes observed at energies less than $\sim$ 2 meV discussed in the main paper are due to interactions between the Yb^{3+} within each tetrahedron.

VI. THEORETICAL DETAILS

A. Model

For completeness, we state our model and conventions in more detail. We consider the effective anistoropic exchange model in the local basis defined as

$$H_{\text{eff}} \equiv \sum_{i=1}^{4} \sum_{j<i} \left[J_{zz} S_i^z S_j^z - J_{\pm} \left(S_i^+ S_j^- + S_i^- S_j^+ \right) + J_{\pm\pm} \left(\gamma_{ij} S_i^+ S_j^+ + \text{h.c} \right) + J_{z\pm} \left(\zeta_{ij} \left[S_i^z S_j^+ + S_i^+ S_j^z \right] + \text{h.c} \right) \right] - \mu_B \mathbf{B} \cdot \sum_{i=1}^{4} \left[g_{\pm} \left(\hat{\mathbf{x}}_i S_i^x + \hat{\mathbf{y}}_i S_i^y \right) + g_z \hat{\mathbf{z}}_i S_i^z \right], \tag{S1}$$

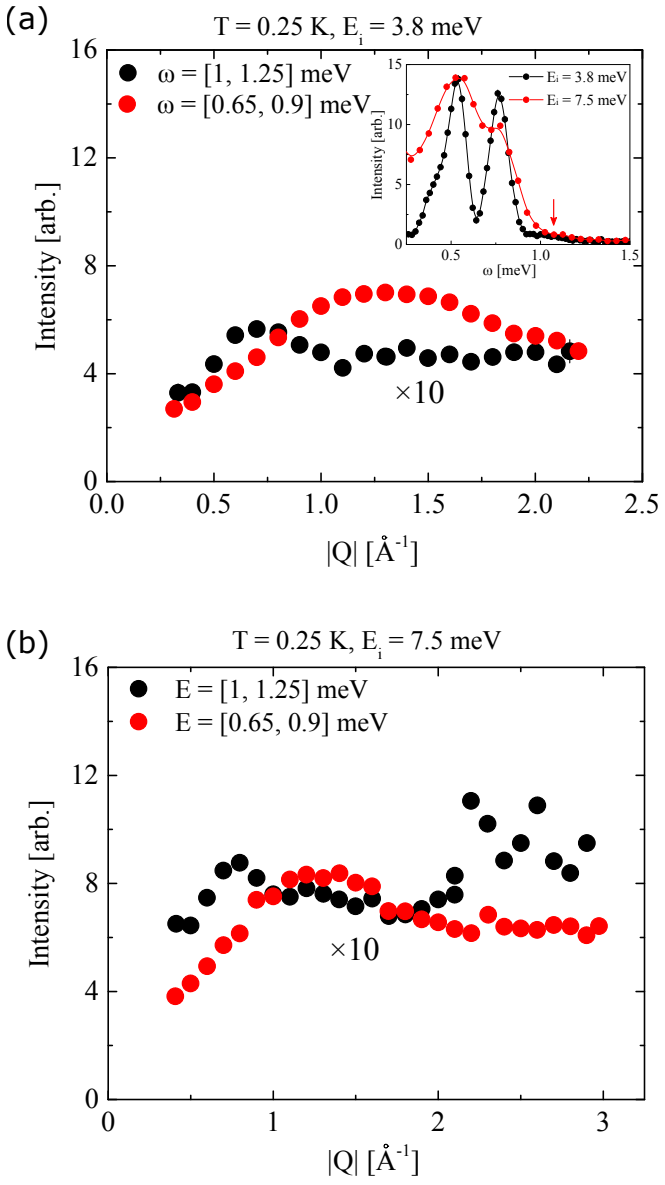

FIG. S5. Wave vector $|\mathbf{Q}|$ dependent neutron scattering intensity averaged over $\omega = [0.65, 0.9]$ meV (red points) and $\omega = [1, 1.25]$ meV (black points), measured at 0.25 K with $E_i = 3.8$ meV (a) and $E_i = 7.5$ meV (b), respectively. The error bars are smaller than the data points. Shown in the inset of (a) is the energy dependent intensity averaged over the wave-vector range $1.25\text{Å}^{-1} < |\mathbf{Q}| < 1.35\text{Å}^{-1}$ at 0.25 K for $E_i = 3.8$ meV and $E_i = 7.5$ meV. The arrow indicates the weak and broad feature around 1 meV.

with four symmetry allowed exchanges J_{zz}, $J_{\pm}$, $J_{\pm\pm}$ and $J_{z\pm}$ and external magnetic field $\mathbf{B}$. The complex bond phase factors γ_{ij} and $\zeta_{ij} = -\gamma_{ij}^*$ depend only on the basis sites they connect and thus can be expressed as a matrix

$$\gamma = \begin{pmatrix} 0 & +1 & \omega & \omega^2 \\ +1 & 0 & \omega^2 & \omega \\ \omega & \omega^2 & 0 & +1 \\ \omega^2 & \omega & +1 & 0 \end{pmatrix}, \tag{S2}$$

where $\omega = e^{2\pi i/3}$. The magnetic field is coupled directly to the effective moment on each Yb^{3+} site, defined as

$$\boldsymbol{\mu}_i \equiv \mu_B \left[g_{\pm} \left(\hat{\mathbf{x}}_i S_i^x + \hat{\mathbf{y}}_i S_i^y \right) + g_z \hat{\mathbf{z}}_i S_i^z \right], \tag{S3}$$

where g_z and $g_{\pm}$ are the g-factors in the local [111] direction and in the plane perpendicular to it. These local axes are defined as

$$\begin{aligned}
\hat{\mathbf{z}}_1 &= \frac{1}{\sqrt{3}}(+\hat{\mathbf{x}} + \hat{\mathbf{y}} + \hat{\mathbf{z}}), & \hat{\mathbf{x}}_1 &= \frac{1}{\sqrt{6}}(-2\hat{\mathbf{x}} + \hat{\mathbf{y}} + \hat{\mathbf{z}}), \\
\hat{\mathbf{z}}_2 &= \frac{1}{\sqrt{3}}(+\hat{\mathbf{x}} - \hat{\mathbf{y}} - \hat{\mathbf{z}}), & \hat{\mathbf{x}}_2 &= \frac{1}{\sqrt{6}}(-2\hat{\mathbf{x}} - \hat{\mathbf{y}} - \hat{\mathbf{z}}), \\
\hat{\mathbf{z}}_3 &= \frac{1}{\sqrt{3}}(-\hat{\mathbf{x}} + \hat{\mathbf{y}} - \hat{\mathbf{z}}), & \hat{\mathbf{x}}_3 &= \frac{1}{\sqrt{6}}(+2\hat{\mathbf{x}} + \hat{\mathbf{y}} - \hat{\mathbf{z}}), \\
\hat{\mathbf{z}}_4 &= \frac{1}{\sqrt{3}}(-\hat{\mathbf{x}} - \hat{\mathbf{y}} + \hat{\mathbf{z}}), & \hat{\mathbf{x}}_4 &= \frac{1}{\sqrt{6}}(+2\hat{\mathbf{x}} - \hat{\mathbf{y}} + \hat{\mathbf{z}}),
\end{aligned} \tag{S4}$$

where $\hat{\mathbf{y}}_i = \hat{\mathbf{z}}_i \times \hat{\mathbf{x}}_i$.

Equivalently, this model can be expressed in *global* quantization axes [S8]. We thus define a global pseudo-spin operator $\tilde{\mathbf{S}}_i$ for each Yb^{3+} site as

$$\tilde{\mathbf{S}}_i \equiv \hat{\mathbf{x}}_i S_i^x + \hat{\mathbf{y}}_i S_i^y + \hat{\mathbf{z}}_i S_i^z. \tag{S5}$$

In this basis the anisotropic exchange model can be written

$$H_{\text{eff}} \equiv \sum_{j=1}^{4} \sum_{i<j} \tilde{\mathbf{S}}_i^{\mathsf{T}} \mathbf{J}_{ij} \tilde{\mathbf{S}}_j, \tag{S6}$$

where the exchange matrices $\mathbf{J}_{ij}$ are defined as

$$\begin{aligned}
\mathbf{J}_{12} &= \begin{pmatrix} J_2 & J_4 & J_4 \\ -J_4 & J_1 & J_3 \\ -J_4 & J_3 & J_1 \end{pmatrix}, & \mathbf{J}_{13} &= \begin{pmatrix} J_1 & -J_4 & J_3 \\ J_4 & J_2 & J_4 \\ J_3 & -J_4 & J_1 \end{pmatrix}, \\
\mathbf{J}_{14} &= \begin{pmatrix} J_1 & J_3 & -J_4 \\ J_3 & J_1 & -J_4 \\ J_4 & J_4 & J_2 \end{pmatrix}, & \mathbf{J}_{23} &= \begin{pmatrix} J_1 & -J_3 & J_4 \\ -J_3 & J_1 & -J_4 \\ -J_4 & J_4 & J_2 \end{pmatrix}, \\
\mathbf{J}_{24} &= \begin{pmatrix} J_1 & J_4 & -J_3 \\ -J_4 & J_2 & J_4 \\ -J_3 & -J_4 & J_1 \end{pmatrix}, & \mathbf{J}_{34} &= \begin{pmatrix} J_2 & -J_4 & J_4 \\ J_4 & J_1 & -J_3 \\ -J_4 & -J_3 & J_1 \end{pmatrix}.
\end{aligned} \tag{S7}$$

These two different parametrizations are related as

$$\begin{aligned}
J_1 &= \frac{1}{3}\left(+4J_{\pm} + 2J_{\pm\pm} + 2\sqrt{2}J_{z\pm} - J_{zz}\right), \\
J_2 &= \frac{1}{3}\left(-4J_{\pm} + 4J_{\pm\pm} + 4\sqrt{2}J_{z\pm} + J_{zz}\right), \\
J_3 &= \frac{1}{3}\left(-2J_{\pm} - 4J_{\pm\pm} + 2\sqrt{2}J_{z\pm} - J_{zz}\right), \\
J_4 &= \frac{1}{3}\left(-2J_{\pm} + 2J_{\pm\pm} - \sqrt{2}J_{z\pm} - J_{zz}\right).
\end{aligned} \tag{S8}$$

As discussed in the main text, the exchange J_4 can be interpreted as a Dzyaloshinskii-Moriya (DM) interaction. Specifically, for $J_1 = J_2 \equiv J$ and $J_3 = 0$ we can write

$$H_{\text{eff}} = \sum_{j=1}^{4} \sum_{i<j} \left[J\tilde{\mathbf{S}}_i \cdot \tilde{\mathbf{S}}_j + \mathbf{D}_{ij} \cdot \left(\tilde{\mathbf{S}}_i \times \tilde{\mathbf{S}}_j \right) \right], \tag{S9}$$

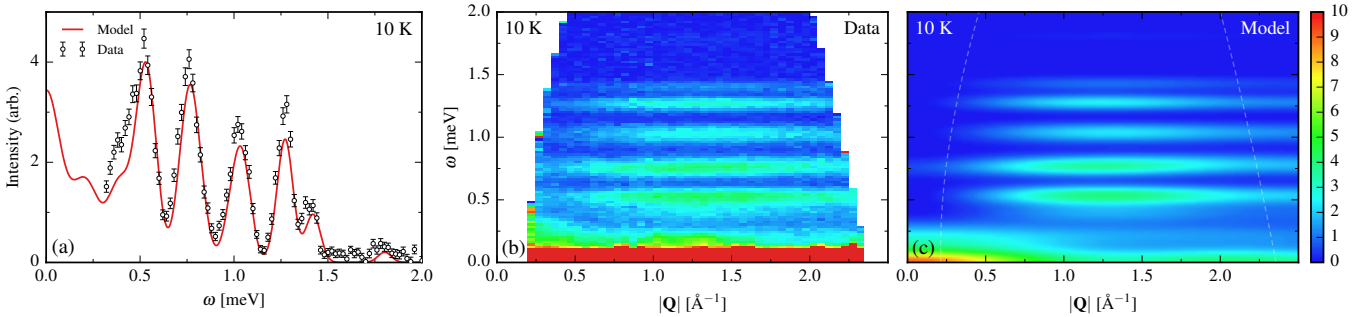

FIG. S6. Inelastic neutron scattering data (E_i=3.8 meV) and comparison to theoretical model at (a-c) 10 K. The overall theoretical intensity scale was fit using the INS cut at 0.25 K. A Gaussian broadening with energy dependence following the experimental energy resolution function (shown in Fig. S7) was included in the theoretical calculation. (a) Cut of INS data averaged over the window 1.25Å^{-1} < |**Q**| < 1.35Å^{-1}. Results for the best fit single tetrahedron model of the main text are shown. (b) Intensity map of powder averaged INS data. The excitations are nearly dispersion free over the full |**Q**| range. (c) Model calculations for the best fit single tetrahedron model. The Yb^{3+} form factor was evaluated in the dipole approximation, as given in Ref. [S4].

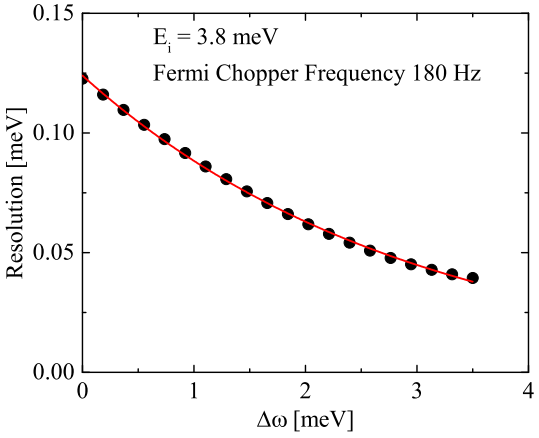

FIG. S7. HYSPEC resolution as a function of the energy transfer $\Delta\omega$, with incident energy E_i = 3.8 meV and Fermi chopper frequency of 180 Hz. The red line is the fit to the empirical equation $y = Ae^{-\Delta\omega/\Gamma}$ with A = 0.12398 ± 0.0004 meV, and Γ = 2.95111 ± 0.02144 meV.

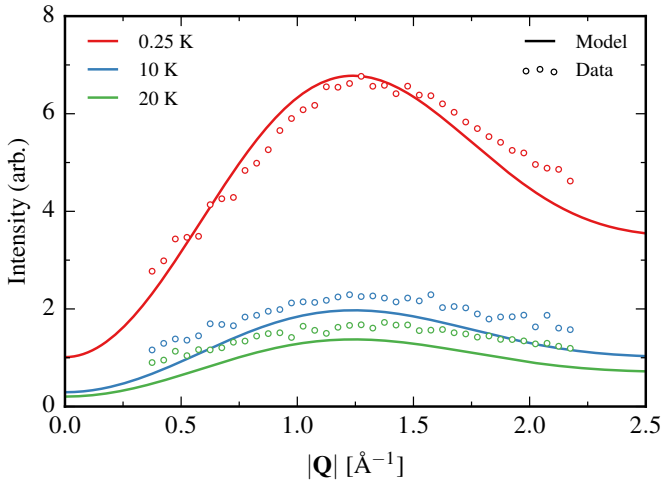

FIG. S8. The |**Q**| dependence of the inelastic neutron scattering data for $Ba_3Yb_2Zn_5O_{11}$, averaged over the excitation in the energy window 0.65 meV < ω < 0.9 meV.

where the DM vectors are defined as $\mathbf{D}_{ij} \equiv D\hat{\mathbf{D}}_{ij}$ with magnitude $D = \sqrt{2}J_4$ and directions

$$\hat{\mathbf{D}}_{12} = \frac{-\hat{\mathbf{y}}+\hat{\mathbf{z}}}{\sqrt{2}}, \quad \hat{\mathbf{D}}_{13} = \frac{+\hat{\mathbf{x}}-\hat{\mathbf{z}}}{\sqrt{2}}, \quad \hat{\mathbf{D}}_{14} = \frac{-\hat{\mathbf{x}}+\hat{\mathbf{y}}}{\sqrt{2}},$$
$$\hat{\mathbf{D}}_{23} = \frac{-\hat{\mathbf{x}}-\hat{\mathbf{y}}}{\sqrt{2}}, \quad \hat{\mathbf{D}}_{24} = \frac{+\hat{\mathbf{x}}+\hat{\mathbf{z}}}{\sqrt{2}}, \quad \hat{\mathbf{D}}_{34} = \frac{-\hat{\mathbf{y}}-\hat{\mathbf{z}}}{\sqrt{2}}. \quad \text{(S10)}$$

With these definitions $J_4 > 0$ corresponds to the so-called direct case, while $J_4 < 0$ corresponds to the indirect case [S9].

1. *Ground state of tetrahedron*

Here we explicitly give the ground state E doublet, $|\pm\rangle$ for the best fit parameters discussed in the main text. We present these wave-functions using the basis states given in Ref. [S10] for the case of effective spin-1/2 degrees of freedom. One finds

$$|\pm\rangle = 0.244|E_\pm^{(1)}\rangle \mp 0.798|E_\pm^{(2)}\rangle - 0.551|E_\mp^{(3)}\rangle \quad \text{(S11)}$$

where we have chosen the overall phase so that the coefficient of $|E_\pm^{(1)}\rangle$ is real and positive.

B. Observables

The effective single tetrahedron model can be numerically diagonalized exactly and all observable quantities can be directly computed. Below we outline how each observable is computed and compared with the respective experimental results.

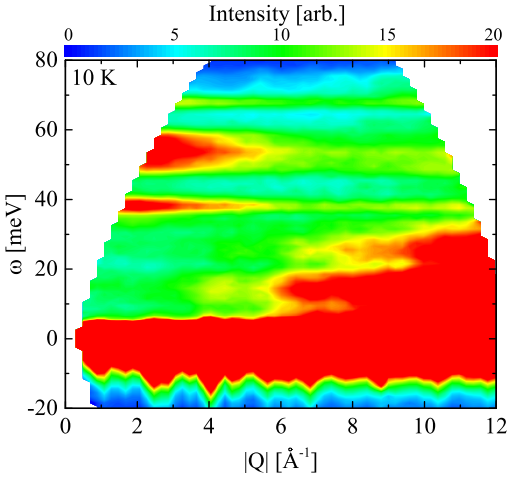

FIG. S9. Intensity map of the inelastic neutron scattering data from $Ba_3Yb_2Zn_5O_{11}$ with $E_i = 100$ meV at 10 K . The data shows three crystal field excitations at 38, 54, and 67 meV.

1. *Specific heat*

As the lattice contribution has been subtracted in Ref. [S1] using the structural analog $Ba_3Lu_2Zn_5O_{11}$, we simply compute the magnetic contribution directly from the model. This is straightforwardly

$$C = \frac{1}{4}\left(\frac{\langle H_{\rm eff}^2\rangle - \langle H_{\rm eff}\rangle^2}{k_B T^2}\right), \tag{S12}$$

where $\langle O\rangle = \mathrm{tr}[Oe^{-\beta H_{\rm eff}}]/\mathrm{tr}[e^{-\beta H_{\rm eff}}]$ denotes a thermal average. While the lattice subtraction seems robust, we only use the specific heat data of Kimura *et al.* [S1] below $T < 5$ K to minimize any possible bias from this procedure.

2. *Susceptibility*

We compute the magnetic susceptibility by emulating the experimental procedure of Kimura *et al.* [S1]. We thus add a small magnetic field with $|\mathbf{B}| = 0.1$ T and the compute magnetization, $\boldsymbol{\mu} \equiv 1/4\sum_{i=1}^{4}\boldsymbol{\mu}_i$, in the effective single tetrahedron model. To better compare to the experimental results, we need to include Van Vleck contributions from the higher crystal field levels and the diamagnetic susceptibility from the Yb^{3+} core electrons. At these low temperatures, we treat this as a constant shift χ_0 to be added to χ. Estimates from Ref. [S1] place these contributions at roughly $\chi_0 \sim 6.9\cdot 10^{-3}$ emu/(mol Yb), though we leave χ_0 as a free parameter in our analysis. As we will see below, the fitted value of χ_0 agrees well with this theoretical estimate. In total the susceptibility, χ, is given by

$$\chi \equiv \mu_0|\langle\boldsymbol{\mu}\rangle|/|\mathbf{B}| + \chi_0, \tag{S13}$$

where $\langle\boldsymbol{\mu}\rangle$ is the magnetization computed in the effective single tetrahedron model in the presence of the magnetic field $\mathbf{B}$. Due to the cubic symmetry, the susceptibility is isotropic and thus the direction $\hat{\mathbf{B}}$ of this applied field is unimportant. We have verified that this field is well within the linear regime, with essentially no difference in computing χ with an extremely small field of $|\mathbf{B}| = 10^{-3}$ T rather than $|\mathbf{B}| = 0.1$ T.

3. *Magnetization*

To compare to the magnetization data of Kimura *et al.* [S1] at larger fields, we compute the magnetization itself as a function of field. As in computing the susceptibility, the χ_0 shift contributes a linear correction to magnetization computed directly from the single tetrahedron model. Explicitly, the total magnetization $\mathbf{M}$ per Yb^{3+} is given as

$$\mathbf{M} \equiv \langle\boldsymbol{\mu}\rangle + \chi_0\mathbf{B}/\mu_0, \tag{S14}$$

where $\langle\boldsymbol{\mu}\rangle$ is the magnetization computed in the effective single tetrahedron model. Unlike when computing the susceptibility, the magnetization measurements of Ref. [S1] go beyond the linear regime and thus $\langle\boldsymbol{\mu}\rangle$ *does* depend on the field direction $\hat{\mathbf{B}}$. To emulate the inherent averaging in the powder samples, we consider fields with arbitrary direction $\hat{\mathbf{B}}$ and fixed magnitude $|\mathbf{B}|$. For each $\mathbf{B}$ we then compute $\hat{\mathbf{B}}\cdot\mathbf{M}$ and integrate over field directions $\hat{\mathbf{B}}$ to obtain the contribution to the powder averaged magnetization.

4. *Inelastic neutron scattering*

The inelastic neutron scattering intensity is given by

$$I(\mathbf{Q},\omega) = I_0\frac{|\mathbf{k}'|}{|\mathbf{k}|}\sum_{\alpha\beta}\left(\delta_{\alpha\beta} - \hat{Q}_\alpha\hat{Q}_\beta\right)F(|\mathbf{Q}|)^2\mathcal{S}^{\alpha\beta}(\mathbf{Q},\omega), \tag{S15}$$

where $\mathbf{k}$, $\mathbf{k}'$ are the initial and final neutron momenta, $F(Q)$ is the form factor for Yb^{3+} [S4] and I_0 is a normalization factor. The dynamical structure factor for a single tetrahedron, $\mathcal{S}^{\alpha\beta}(\mathbf{Q},\omega)$, is given as

$$\mathcal{S}^{\alpha\beta}(\mathbf{Q},\omega) = \sum_{nn'}\frac{e^{-\beta E_n}}{Z}\langle n|\mu^\alpha_{-\mathbf{Q}}|n'\rangle\langle n'|\mu^\beta_{\mathbf{Q}}|n\rangle\,\delta(\omega - E_{n'} + E_n),$$

where $|n\rangle$, E_n are the eigenstates and energies of the single tetrahedron model $H_{\rm eff}$ and Z is the partition function. The operators $\boldsymbol{\mu}_{\mathbf{Q}}$ are defined as

$$\boldsymbol{\mu}_{\mathbf{Q}} \equiv \frac{1}{4}\sum_{i=1}^{4}e^{-i\mathbf{Q}\cdot\mathbf{r}_i}\boldsymbol{\mu}_i, \tag{S16}$$

where $\boldsymbol{\mu}_i$ and $\mathbf{r}_i$ are the Yb^{3+} moments and site positions. The prefactor $|\mathbf{k}'|/|\mathbf{k}| = (1-\omega/E_i)^{1/2}$ and reduces the relative intensity of some higher lying features. For the INS data we are interested in, one has $E_i = 3.8$ meV and this only is significant at high energies. We consider the powder averaged cross section

$$I_{\rm avg}(Q,\omega) \equiv \int d\hat{\mathbf{Q}}\, I(Q\hat{\mathbf{Q}},\omega). \tag{S17}$$

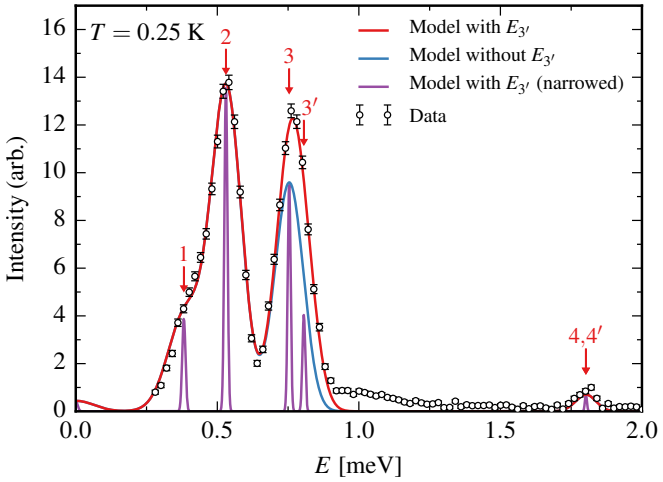

FIG. S10. Comparison of the inelastic neutron scattering intensity to the model with the $E_{3'}$ level included and excluded. With the $E_{3'}$ level excluded, the intensity near ~ 0.8 meV is not fully accounted for. To show that the mode at ~ 0.8 meV is composed of both the E_3 and $E_{3'}$ levels we have shown the predicted model intensity with higher energy resolution, clearly resolving the two levels.

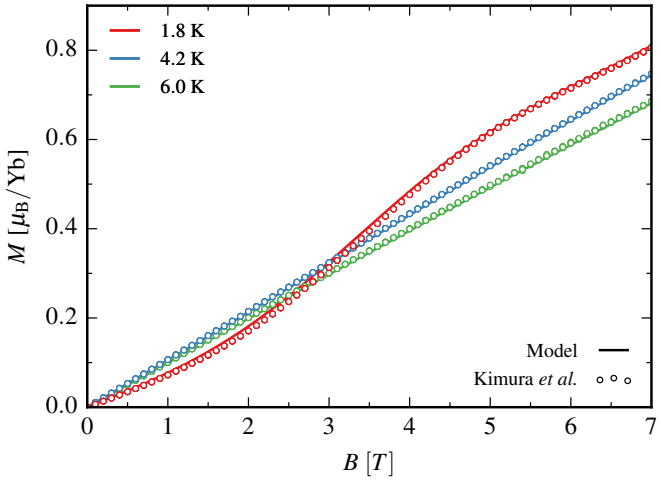

FIG. S11. Comparison of the magnetization data of Kimura *et al.* [S1] at $T = 1.8$ K, 4.2 K and 6.0 K to the model calculations for the best fit parameters. The Van Vleck and core diamagnetic contributions, χ_0, fitted in the susceptibility also contribute to the magnetization.

Due to the isolated tetrahedra, strictly $I_{\rm avg}(Q,\omega)$ has features flat in $|\mathbf{Q}|$, and sharp in energy. At low temperature, these simply reflect transitions from the ground state to the excited levels. Additional information resides in the intensity variations. To compare with the experimental data, we include an overall scale factor, I_0, to represent the arbitrary experimental intensity scale. To emulate the finite experimental energy resolution, we convolve $I_{\rm avg}(Q,\omega)$ with Gaussians of finite width. The experimental energy resolution is energy dependent, varying approximately as $\sim Ae^{-\omega/\Gamma}$ as given in Fig. S7. To incorporate this, the width of this Gaussian broadening made energy dependent as well, following this experimental form. However, as the observed levels are somewhat broader than the experimental limit, we allow the overall scale of this energy dependent width, denoted as $A^{(\rm fit)}$, to vary in the theoretical calculation while keeping the experimentally determined value for Γ.

We note here that, due to the finite experimental resolution, some of the transitions strongly overlap. This is most apparent in the E_4 and $E_{4'}$ levels where the energy difference is $\sim 10^{-4}$ meV, but is also an issue for the E_3 and $E_{3'}$ levels. We illustrate this in Fig. (S10), highlighting the contribution of the $E_{3'}$ level to the intensity of the mode near ~ 0.8 meV. With the $E_{3'}$ level removed, the intensity of this mode no longer matches the experimental data.

5. *Ground doublet composition*

In this section we comment on the difference between the g-factors found in our study, and those obtained from the analysis of the crystal field excitations reported in Ref. [S7]. As we work directly in the subspace of the crystal field ground doublets, the only point of comparison is through these g-factors. Ref. [S7] reports values (in our notation) of $(g_\pm, g_z) = (3.31, 2.35)$, while we found values $(g_\pm, g_z) = (2.36, 3.07)$.

We note that the fitting of the crystal field parameters from the high energy Yb^{3+} levels is somewhat unconstrained. In is unclear whether the experimental constraints are sufficient to uniquely pin down the 6 free parameters in the crystal field potential. Furthermore, the higher crystal field levels are likely to be split by intra-tetrahedron interactions in the same fashion as the ground doublet. As seen in this main text, this splitting is on the order of $\sim$ 2 meV or so (possibly larger in these higher energy doublets). This would both broaden and shift the higher crystal field levels and likely skew the results of any crystal field analysis. Indeed, in the crystal field excitation data presented in Fig. S9 the excitation near 54 meV is extremely broad and shows evidence of sub-levels. This feature is attributed to phonon coupling in Ref. [S7], which could introduce similar uncertainties. Given the already somewhat under-constrained nature of the fitting, this may have strong effects on the obtained crystal field parameters and thus the ground doublet composition and g-factors. For these reasons, we believe our determination of the g-factors, obtained directly from the low-energy physics, may provide a more reliable estimate than a crystal field analysis of Ref. [S7].

That being said, there is some non-trivial agreement between our results and those of Ref [S7]. For Yb^{3+} ions with Γ_4 ground state doublets, as we have here, the two g-factors essentially determine the composition of the ground state doublet. Generically, a Γ_4 doublet for a $J = 7/2$ system can be written as

$$|\pm\rangle \equiv \pm\alpha\,|\pm 7/2\rangle - \beta\,|\pm 1/2\rangle \pm \gamma\,|\mp 5/2\rangle \qquad \text{(S18)}$$

where α, β and γ are real numbers that satisfy $\alpha^2+\beta^2+\gamma^2 = 1$. We define the g-factors via the magnetic moment $\boldsymbol{\mu}_i$ as

$$\boldsymbol{\mu}_i \equiv \mu_{\rm B} g_J\,(P\mathbf{J}_i P) = \mu_{\rm B}\left(g_\pm \hat{\mathbf{x}}_i S_i^x + g_\pm \hat{\mathbf{y}}_i S_i^y + g_z \hat{\mathbf{z}}_i S_i^z\right) \qquad \text{(S19)}$$

where $g_J = 8/7$ is the Landé g-factor for the $^2F_{7/2}$ manifold for Yb^{3+} and P projects into the crystal field ground doublets. This gives three equations

$$g_\pm/g_J = 7\alpha^2 + \beta^2 - 5\gamma^2 \tag{S20a}$$
$$g_z/g_J = 4\beta^2 - 2\sqrt{7}\alpha\gamma \tag{S20b}$$
$$1 = \alpha^2 + \beta^2 + \gamma^2 \tag{S20c}$$

While the signs are not uniquely fixed, the magnitudes of α, β and γ, and thus the composition of the ground doublet, are determined by these three equations. For $(g_\pm, g_z) = (2.36, 3.07)$ we have the ground doublet $|\pm\rangle$ with composition (following the signs in Ref. [S7])

$$|\pm\rangle = \mp 0.561\,|\pm 7/2\rangle - 0.807\,|\pm 1/2\rangle \mp 0.183\,|\mp 5/2\rangle \tag{S21}$$

This is qualitatively similar to the doublet $|\pm\rangle = \mp 0.537\,|\pm 7/2\rangle - 0.805\,|\pm 1/2\rangle \pm 0.251\,|\mp 5/2\rangle$ found in Ref. [S7]. The only qualitative difference lies in the sign and weight of the $|\mp 5/2\rangle$ states.

C. Fitting

As discussed in the main text, to fit the experimental data we use the specific heat, susceptibility and a cut of inelastic neutron scattering data averaged over the range $1.25\text{Å}^{-1} < |\mathbf{Q}| < 1.35\text{Å}^{-1}$. Here we present explicit details of our fitting methodology. We denote the specific heat data of Kimura *et al.* [S1] as a set of temperatures $T_n^{(\text{exp},C)}$ and values $C_n^{(\text{exp})}$ where n labels each data point. As discussed in the main text, we only use data points with $T < 5$ K to minimize possible issues with the lattice subtraction. Similarly for the susceptibility, we define $T_n^{(\text{exp},\chi)}$ and $\chi_n^{(\text{exp})}$ (taking all points with $T < 30$ K) and for the INS cut $\omega_n^{(\text{exp},\chi)}$ and $I_n^{(\text{exp})}$ (taking all points with 0.25 meV $< \omega <$ 2 meV in the $T = 0.25$ K cut). For each temperature T or energy ω we can compute the theoretical values, yielding $C_n^{(\text{theo})}$, $\chi_n^{(\text{theo})}$ and $I_n^{(\text{theo})}$ as outlined in the previous section. Thinking of these sets of observations and theoretical values as vectors, we define the discrepancy

$$\epsilon_X \equiv |\mathbf{X}^{(\text{exp})} - \mathbf{X}^{(\text{theo})}|/|\mathbf{X}^{(\text{exp})}|, \tag{S22}$$

where $X = C, \chi$ or I. To find the best fit of the experimental data, we minimize the sum of these differences $\epsilon_{\text{tot}} \equiv \epsilon_C + \epsilon_\chi + \epsilon_I$. In total we have nine fitting parameters:

1. The exchanges J_{zz}, $J_\pm$, $J_{\pm\pm}$ and $J_{z\pm}$
2. The g-factors, g_z and $g_\pm$
3. The susceptibility shift χ_0
4. The intensity scale of the INS spectrum I_0 and the scale of the Gaussian energy broadening $A^{(\text{fit})}$

We used standard minimization algorithms to find the best fit presented in the main text. To aid in finding the global minimum, the minimization process was repeated for several thousand random initial conditions. To be specific regarding the initialization, the four exchanges were drawn from uniform distributions covering the range $[-0.3, +0.3]$ meV, each g-factor from the range $[1, 3]$ and χ_0 susceptibility shift from the range $[6, 8] \cdot 10^{-3}$ emu/(mol Yb). The neutron intensity was always initialized to $I_0 = 0.01$, while the energy width $A^{(\text{fit})}$ was initialized with the experimental value $A = 0.124$ meV. In the main text, we reported the exchanges and g-factors. The remaining parameters for the best fit are given as

$$I_0 = 0.012, \quad A^{(\text{fit})}/A = 1.24, \quad \chi_0 = 6.75 \cdot 10^{-3}\ \text{emu/(mol Yb)}.$$

We see that the susceptibility shift χ_0 compares favorably with the expected theoretical value [S1]. We note that the required scale to the energy broadening is somewhat larger than the experimental resolution, by about 25%, as can be seen directly in the INS cuts at 0.25 K. Additional comparisons of the experimental results and the theoretical model are shown in Fig. S6 (INS at 10 K), Fig. S11 (magnetization) and Fig. S8 ($|\mathbf{Q}|$ dependence of INS intensity).

While the best fit parameters found are qualitatively unique, they can vary somewhat if one changes details of the fitting procedure. For example, by changing temperature ranges used in C or χ, or assigning different relative weights to each data set. The most sensitive of the parameters is J_{zz}, which can vary by as much as 0.02 to 0.04 meV, while the other parameters can vary by 10% or so. None of these variations change the qualitative picture that emerges from our analysis; in the global basis the system predominantly antiferromagnetic Heisenberg and (indirect) DM interactions and small symmetric anisotropies.

[S1] K. Kimura, S. Nakatsuji, and T. Kimura, Phys. Rev. B **90**, 060414 (2014).

[S2] A. Huq, J. P. Hodges, L. Heroux, and O. Gourdon, Zeitschrift fur Kristallographie Proceedings **1**, 127 (2011).

[S3] J. Rodriguez-Carvajal, Physica B: Condensed Matter **192**, 55 (1993).

[S4] A. J. C. Wilson, *International Tables for Crystallography: Mathematical, physical, and chemical tables*, Vol. 3 (International Union of Crystallography, 1992).

[S5] B. Winn, U. Filges, V. O. Garlea, M. Graves-Brook, M. Hagen, C. Jiang, M. Kenzelmann, L. Passell, S. M. Shapiro, X. Tong, and I. Zaliznyak, in *EPJ Web of Conferences*, Vol. 83 (EDP Sciences, 2015) p. 03017.

[S6] D. L. Abernathy, M. B. Stone, M. J. Loguillo, M. S. Lucas, O. Delaire, X. Tang, J. Y. Y. Lin, and B. Fultz, Review of Scientific Instruments **83**, 015114 (2012).

[S7] T. Haku, M. Soda, M. Sera, K. Kimura, S. Itoh, T. Yokoo, and T. Masuda, (2015), arXiv:1510.03049 [cond-mat.mtrl-sci].
[S8] H. Yan, O. Benton, L. D. C. Jaubert, and N. Shannon, (2013), arXiv:1311.3501 [cond-mat.str-el].
[S9] B. Canals, M. Elhajal, and C. Lacroix, Phys. Rev. B **78**, 214431 (2008).
[S10] S. H. Curnoe, Phys. Rev. B **75**, 212404 (2007).